# Testing of a Cell-Integrated Semi-Lagrangian Semi-Implicit Nonhydrostatic Atmospheric Solver (CSLAM-NH) with Idealized Orography

MAY WONG*

*University of British Columbia, Vancouver, British Columbia, Canada*

WILLIAM C. SKAMAROCK, PETER H. LAURITZEN, AND JOSEPH B. KLEMP

*National Center for Atmospheric Research,[+] Boulder, Colorado*

ROLAND B. STULL

*University of British Columbia, Vancouver, British Columbia, Canada*

(Manuscript received 11 February 2014, in final form 5 December 2014)

ABSTRACT

A recently developed cell-integrated semi-Lagrangian (CISL) semi-implicit nonhydrostatic atmospheric solver that uses the conservative semi-Lagrangian multitracer (CSLAM) transport scheme is extended to include orographic influences. With the introduction of a new semi-implicit CISL discretization of the continuity equation, the nonhydrostatic solver, called CSLAM-NH, has been shown to ensure inherently conservative and numerically consistent transport of air mass and other scalar variables, such as moisture and passive tracers. The extended CSLAM-NH presented here includes two main modifications: transformation of the equation set to a terrain-following height coordinate to incorporate orography and an iterative centered-implicit time-stepping scheme to enhance the stability of the scheme associated with gravity wave propagation at large time steps. CSLAM-NH is tested for a suite of idealized 2D flows, including linear mountain waves (dry), a downslope windstorm (dry), and orographic cloud formation.

## 1. Introduction

Semi-Lagrangian semi-implicit (SLSI) schemes have been widely used in climate and numerical weather prediction (NWP) models since the pioneering work of Robert (1981) and Robert et al. (1985). The fully compressible nonhydrostatic equations permit fast-moving waves that limit the model time step size. The combination of a semi-Lagrangian advection scheme with semi-implicit treatment of these waves allows for larger stable time steps, and therefore, increased computational efficiency. Conservative semi-Lagrangian advection schemes, also known as cell-integrated semi-Lagrangian (CISL) transport schemes, are finite-volume methods that inherently conserve mass by tracking individual grid cells each time step (Rancic 1992; Laprise and Plante 1995; Machenhauer and Olk 1997; Zerroukat et al. 2002; Nair and Machenhauer 2002; Lauritzen et al. 2010). CISL transport schemes allow for locally (and thus globally) conservative transport of total fluid mass (such as dry air in the atmosphere) and constituent (i.e., moisture and tracer) mass.

However, some CISL schemes lack consistency between the numerical representation of the total dry air mass conservation, which we will refer to as the continuity equation, and constituent mass conservation equations (Jöckel et al. 2001; Zhang et al. 2008; Wong et al. 2013). Numerical consistency in the discrete tracer conservation equation requires the equation for a constant

* Current affiliation: Pacific Northwest National Laboratory, Richland, Washington.

[+] The National Center for Atmospheric Research is sponsored by the National Science Foundation.

*Corresponding author address:* May Wong, Pacific Northwest National Laboratory, Atmospheric Sciences and Global Change Division, 902 Battelle Blvd., P.O. Box 999, MSIN K9-24, Richland, WA 99352.
E-mail: may.wong@pnnl.gov

DOI: 10.1175/MWR-D-14-00059.1

tracer field to correspond numerically to the discrete mass continuity equation; this consistency ensures that an initially spatially uniform passive tracer field will remain so.

To allow for large advection time steps, Lauritzen et al. (2010) developed a CISL transport scheme called the conservative semi-Lagrangian multitracer (CSLAM) transport scheme. The CSLAM scheme has recently been implemented in the National Center for Atmospheric Research (NCAR) High-Order Methods Modeling Environment (HOMME) and was found to be an efficient and highly scalable transport scheme for atmospheric tracers (Erath et al. 2012). To ensure consistent numerical representations of the continuity equation and other scalar conservation equations, Wong et al. (2014) proposed a new discretization of the semi-implicit CISL continuity equation using CSLAM. They showed that the new formulation can be straightforwardly extended to the scalar conservation equations in a fully consistent manner. Wong et al. (2013) also showed that any discrepancy between the numerical schemes can lead to spurious generation or removal of scalar mass. We refer to this nonhydrostatic atmospheric solver with conservative and consistent transport as CSLAM-NH.

Idealized 2D benchmark test cases for a density current, gravity wave, as well as a squall line, using CSLAM-NH have been performed in Wong et al. (2014). These test cases used flat bottom boundary conditions for simplicity. In the real atmosphere, the bottom fluid boundary is often not flat. Mountains act as a stationary forcing and generate horizontally and vertically propagating internal gravity waves in the atmosphere. Under certain atmospheric conditions they can also induce highly nonlinear flows such as wave amplification and breaking. Numerical simulations of these mountain waves have been extensively studied by many (e.g., Klemp and Lilly 1978; Peltier and Clark 1983; Durran and Klemp 1983; Durran 1986; Schär et al. 2002) and several of these cases have become benchmark tests in model development and intercomparison studies (e.g., Pinty et al. 1995; Bonaventura 2000; Xue et al. 2000; Doyle et al. 2000; Melvin et al. 2010). To further develop CSLAM-NH as a viable nonhydrostatic atmospheric solver, we have incorporated orography into the model and have conducted a suite of these mountain-wave cases documented in the literature. The test suite includes linear hydrostatic and nonhydrostatic dry mountain waves, a highly nonlinear dry mountain wave with amplification and overturning of the waves, and a moist mountain flow with cloud and rain formation.

The paper is organized as follows. A model description of CSLAM-NH is given in section 2. In section 3, simulations from the suite of idealized mountain wave tests are presented. Finally, a summary is given in section 4.

## 2. Model description

### a. Governing equations

The major modification to the model prognostic equations described in Wong et al. (2014) is the transformation of the vertical coordinate from geometric height to a terrain-following height coordinate. In addition to this modification, we have also included the treatment of the gravity wave terms in the implicit solver. The previous version of CSLAM-NH solves the buoyancy terms in the vertical momentum equation explicitly using a two time-level extrapolation scheme. For a gravity wave test originally proposed in Skamarock and Klemp (1994), the time-step limit was found to be restricted by the explicit treatment of these buoyancy terms (Wong et al. 2014). To circumvent this time step restriction, an iterative approach is used to include these terms in the implicit solver. We will focus on the description of these two modifications and provide a basic description of the solver [readers are referred to Wong et al. (2014) for a more detailed description].

A height-based coordinate is used to avoid the complication of a time-varying vertical coordinate system, as is the case with mass (pressure) coordinates or Lagrangian vertical coordinates. The use of terrain-following coordinates substantially simplifies the bottom boundary condition when topography is present. For cell-integrated semi-Lagrangian advection, in a geometric height coordinate, approximated departure cell boundaries may intersect the orography and create more complex cell configurations (e.g., more cell edges/vertices, which complicate the subgridcell reconstruction). On a computational grid defined by terrain-following vertical coordinates, however, the lowest cell boundaries will always remain at the surface.

Following Gal-Chen and Somerville (1975), the 2D terrain-following height coordinate $\zeta$ is expressed using the linear transformation:

$$\zeta = z_t \frac{z - h(x)}{z_t - h(x)},$$

where $z(x, \zeta)$ is the physical height, $h(x)$ is the terrain profile, and $z_t$ is the height of the model top [with the bottom defined as $z = h(x)$].

The 2D governing equations expressed in $(x, \zeta)$ coordinates are

$$\frac{\partial u}{\partial t}+\left(u\frac{\partial u}{\partial x}\right)_{\zeta}+\omega\frac{\partial u}{\partial \zeta}=-\frac{1}{\tilde{\rho}_m}\gamma R_d\pi\left[\left(\frac{\partial \Theta'_m}{\partial x}\right)_{\zeta}+\frac{\partial(\zeta_x\Theta'_m)}{\partial\zeta}\right]+F_u, \quad (1)$$

$$\frac{\partial w}{\partial t}+\left(u\frac{\partial w}{\partial x}\right)_{\zeta}+\omega\frac{\partial w}{\partial \zeta}=-\frac{1}{\tilde{\rho}_m}\left[\gamma R_d\pi\frac{\partial(\zeta_z\Theta'_m)}{\partial\zeta}-g\tilde{\overline{\rho}}_d\frac{\pi'}{\overline{\pi}}+g\tilde{\rho}'_m\right]+F_w, \quad (2)$$

$$\frac{\partial\Theta_m}{\partial t}+(\nabla\cdot\mathbf{v}\Theta_m)_{\zeta}=F_{\Theta}, \quad (3)$$

$$\frac{\partial\tilde{\rho}_d}{\partial t}+(\nabla\cdot\mathbf{v}\tilde{\rho}_d)_{\zeta}=0, \quad (4)$$

$$\frac{\partial Q_j}{\partial t}+(\nabla\cdot\mathbf{v}Q_j)_{\zeta}=F_{Q_j}, \quad (5)$$

$$p=p_0\left(\frac{R_d\Theta_m}{p_0}\right)^{\gamma}, \quad (6)$$

where $\mathbf{v}=(u, w)$ is the horizontal and vertical wind components, $\pi=(p/p_0)^{\kappa}$ is the Exner function, $p_0=100$ kPa is the reference pressure, $R_d=287\,\mathrm{J\,kg^{-1}\,K^{-1}}$ is the gas constant for dry air, $c_p=1003\,\mathrm{J\,kg^{-1}\,K^{-1}}$ is the specific heat for dry air at constant pressure, $c_v=717\,\mathrm{J\,kg^{-1}\,K^{-1}}$ is the specific heat of dry air at constant volume, and the ratios $\kappa=R_d/c_p\approx0.286$ and $\gamma=c_p/c_v\approx1.4$. Perturbation variables from a time-independent hydrostatically balanced background state are used to reduce numerical errors in the calculations of the pressure-gradient terms (Klemp et al. 2007). The hydrostatically balanced background state is defined as $d\overline{p}(z)/dz=-\overline{\rho}_d(z)g$. Flux-form variables are coupled to a scaled dry density adjusted to the transformed coordinate, $\tilde{\rho}_d=\rho_d/\zeta_z$ (i.e., $\Theta_m=\tilde{\rho}_d\theta_m$ and $Q_j=\tilde{\rho}_d q_j$). The notations $(\zeta_x, \zeta_z)$ refer to the spatial derivatives of $\zeta$. Perturbation variables (primed) are defined via $\Theta_m=\overline{\rho}_d(z)\overline{\theta}(z)+\Theta'_m$, $\pi=\overline{\pi}+\pi'$, $\rho_d=\overline{\rho}_d(z)+\rho'_d$, and the moist density $\tilde{\rho}_m=\tilde{\rho}_d(1+q_v+q_c+q_r)$, where $q_v$, $q_c$, and $q_r$ are the mixing ratios for water vapor, cloud, and rainwater, respectively. The modified potential temperature $\theta_m$ is defined as $\theta_m=\theta(1+a'q_v)$ where $a'\equiv R_v/R_d\simeq1.61$.

Notations $(\cdot)_{\zeta}$ denote evaluation at constant $\zeta$, and $(\nabla\cdot\mathbf{v}b)_{\zeta}=\delta_x(ub)+\delta_{\zeta}(\omega b)$ for any scalar variable $b$. The variable $\omega=d\zeta/dt$ is the vertical motion perpendicular to the coordinate surface. For simplicity, we assume a nonrotating atmosphere. The terms $F_u$ and $F_w$ represent diffusion, and $F_{\Theta}$ and $F_{Q_j}$ represent diffusion as well as any diabatic source terms from parameterized physics.

The governing equations used in CSLAM-NH follow the approach of Klemp et al. (2007) except that the CSLAM-NH equations use the advective form of the momentum equations [(1) and (2)] so that we can use a traditional semi-Lagrangian discretization. The flux-form advection for potential temperature, density, and moisture–passive scalar variables [(3), (4), and (5), respectively] are solved using the conservative semi-Lagrangian scheme CSLAM. Pressure is a diagnostic variable given by the equation of state in (6). Following Klemp et al. (2007), the pressure-gradient terms are written in terms of potential temperature. The recasting allows for coupling of the implicit pressure-gradient terms with the flux divergence term in the potential temperature equation. The compressible nonhydrostatic equation set is still exact and no approximations have been applied.

### b. *CSLAM—A cell-integrated semi-Lagrangian transport scheme*

When advection terms are evaluated using an Eulerian scheme, the model time step sizes are restricted by the well-known Courant stability condition. To allow for larger advective time steps, the nonhydrostatic solver uses a CISL transport scheme called the CSLAM transport scheme developed by Lauritzen et al. (2010). This inherently conservative (both locally and globally) transport scheme is used to solve the continuity and potential temperature equations, and for transport of any moist species or other tracers.

The stability criterion for the CSLAM transport scheme is limited by the trajectory approximations of the gridcell vertices. To ensure stability in traditional semi-Lagrangian schemes, the Lipschitz stability condition requires that, in 1D, no trajectories in the space–time domain should intersect one another (Smolarkiewicz and Pudykiewicz 1992). In the CSLAM scheme, the stability condition is slightly more lenient in that the trajectories of neighboring vertices may cross, as long as the discrete departure cells remain non-self-intersecting. In all test cases presented here, linear trajectories as described in Wong et al. (2014) are assumed. Figure 1a shows a discrete arrival grid cell (white box) originating from a non-self-intersecting discrete departure cell (gray box) with straight edges that are computed using the approximated displacement over one time step (arrows). The trajectories from the ends of the left cell edge intersect, but as long as the departure cells remain non-self-intersecting, the scheme is stable and ensures global mass conservation. In Fig. 1b, a more

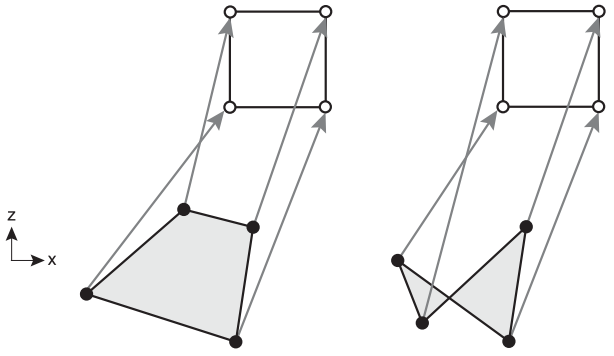


(a) Non-self-intersecting departure cell (b) Self-intersecting departure cell

FIG. 1. Discrete departure cells in CSLAM-NH are approximated using straight edges (shaded in gray). The departure cell vertices (black circles) are computed using backward-in-time trajectories (arrows) from the vertices (white circles) of the Eulerian arrival grid cell (white box). The CSLAM transport scheme is stable as long as the discrete departure grid cells are (a) non-self-intersecting, and becomes problematic if (b) the departure cell self-intersects since the scheme is no longer mass conserving.

distorted flow causes the departure cell to self-intersect. This "twisting" of the departure cell causes adjacent departure cells to overlap. In such a case, the scheme is no longer mass conserving and becomes unstable. The stability and accuracy of the CSLAM scheme in highly deformed flows may be improved by using higher-order trajectory approximations and/or higher-order approximations of departure cell boundaries. One such example is to use the parabolic (curved) departure cell edges that account for acceleration in the trajectory approximations developed by Ullrich et al. (2013). In the present study, we did not test any geometrical definitions other than quadrilateral departure cells, but the option could be explored in the future.

### c. Discretized momentum equations

The momentum equations are solved in a traditional semi-Lagrangian semi-implicit manner, where the total derivatives $du/dt$ and $dw/dt$ are computed using a grid-point interpolation to the departure point. Bicubic Lagrange interpolation is used for all departure point evaluations. The two time-level discretizations of the momentum equations are

$$u_A^{n+1} = u_D^n + \Delta t (F_u)_D^n - \frac{\Delta t}{2}\left\{ \gamma R_d \frac{\overline{\pi}^x}{\tilde{\rho}_m} [(\delta_x \Theta'_m)_\zeta + \delta_\zeta (\zeta_x \overline{\overline{\Theta'_m}^x}^\zeta)] \right\}_D^n - \frac{\Delta t}{2}\left\{ \gamma R_d \frac{\overline{\pi^n}^x}{\tilde{\rho}_m^n} [(\delta_x \Theta'_m)_\zeta + \delta_\zeta (\zeta_x \overline{\overline{\Theta'_m}^x}^\zeta)]_A^{n+1} \right\} \tag{7}$$

and

$$(1+\mu\Delta t) w_A^{n+1} = w_D^n + \Delta t (F_w)_D^n - \frac{\Delta t}{2}\left\{ \gamma R_d \frac{\overline{\pi}^\zeta}{\tilde{\rho}_m} [\delta_\zeta (\zeta_z \Theta'_m)] - \overline{\frac{1}{\tilde{\rho}_m}\left[ g\tilde{\overline{\rho}}_d \frac{\pi'}{\overline{\pi}} - g\tilde{\rho}'_m \right]}^\zeta \right\}_D^n$$
$$- \frac{\Delta t}{2}\left\{ \gamma R_d \frac{\overline{\pi^n}^\zeta}{\tilde{\rho}_m^n} [\delta_\zeta (\zeta_z \Theta'_m)]_A^{n+1} - \overline{\frac{1}{\tilde{\rho}_m^n}\left[ g\tilde{\overline{\rho}}_d \frac{\pi'}{\overline{\pi}} - g\tilde{\rho}'_m \right]_A^{n+1}}^\zeta \right\}, \tag{8}$$

where subscripts $D$ and $A$ denote evaluation at the departure and arrival grid points, respectively, and superscripts denote the time level. The discretization is based on the Arakawa C grid. To reduce gravity wave reflection at the upper boundary, a Rayleigh damping term $-\mu w$ is added to the vertical momentum equation, where the damping coefficient $\mu$ is a function of height $z$ and applied in the top layers of the domain. This damping term shows up as $\mu\Delta t$ on the lhs of the vertical momentum equation in (8). The spatial averaging operators are defined as

$$\overline{(\cdot)}^x = \frac{1}{2}[(\cdot)_{i,k} + (\cdot)_{i+1,k}], \quad \text{and}$$

$$\overline{(\cdot)}^\zeta = \frac{1}{2}[(\cdot)_{i,k} + (\cdot)_{i,k+1}],$$

and gradient operators as

$$\delta_x(\cdot) = \frac{(\cdot)_{i+1,k} - (\cdot)_{i,k}}{\Delta x}, \quad \text{and}$$

$$\delta_\zeta(\cdot) = \frac{(\cdot)_{i,k+1} - (\cdot)_{i,k}}{\Delta \zeta}.$$

The prognostic variable for vertical motion perpendicular to the terrain-following vertical coordinate $\zeta$ is

$$\omega^{n+1} = \zeta_x u^{n+1} + \zeta_z w^{n+1}.$$

We use the following notations to combine the known rhs terms in the momentum equations:

$$R_U \equiv u_D^n + \Delta t(F_u)_D^n - \frac{\Delta t}{2}\left\{\gamma R_d \frac{\overline{\pi}^x}{\tilde{\rho}_m}[(\delta_x \Theta'_m)_\zeta + \delta_\zeta(\zeta_x \overline{\overline{\Theta'_m}^{x}}^{\zeta})]\right\}_D^n,$$

$$R_W \equiv w_D^n + \Delta t(F_w)_D^n - \frac{\Delta t}{2}\left\{\gamma R_d \frac{\overline{\pi}^\zeta}{\tilde{\rho}_m}[\delta_\zeta(\zeta_z \Theta'_m)] - \overline{\frac{1}{\tilde{\rho}_m}\left[g\tilde{\bar{\rho}}_d \frac{\pi'}{\overline{\pi}} - g\tilde{\rho}'_m\right]}^{\zeta}\right\}_D^n,$$

the implicit pressure-gradient terms:

$$\mathrm{PG}_U = -\frac{\Delta t}{2}\left\{\gamma R_d \frac{\overline{\pi^n}^x}{\tilde{\rho}_m^n}[(\delta_x \Theta'_m)_\zeta + \delta_\zeta(\zeta_x \overline{\overline{\Theta'_m}^{x}}^{\zeta})]_A^{n+1}\right\},$$

$$\mathrm{PG}_W = -\frac{\Delta t}{2}\left\{\gamma R_d \frac{\overline{\pi^n}^\zeta}{\tilde{\rho}_m^n}[\delta_\zeta(\zeta_z \Theta'_m)]_A^{n+1}\right\},$$

and the implicit half of the buoyancy term:

$$B_W = \frac{\Delta t}{2}\overline{\frac{1}{\tilde{\rho}_m^n}\left[g\tilde{\bar{\rho}}_d \frac{\pi'}{\overline{\pi}} - g\tilde{\rho}'_m\right]_A^{n+1}}^{\zeta}. \tag{9}$$

The subscripts in the notations denote the momentum equations to which the terms belong. Using (7) and (8), and the notations above, the vertical momentum equation can be rewritten as

$$\omega^{n+1} = \underbrace{\zeta_x R_U + \zeta_z(1+\mu\Delta t)^{-1}(R_W + B_W)}_{R_\Omega} + \zeta_x \mathrm{PG}_U + \zeta_z(1+\mu\Delta t)^{-1}\mathrm{PG}_W. \tag{10}$$

The notation $R_\Omega$ is used here to represent all the known terms plus the implicit buoyancy term in (9).

Often, off-centering of the time-averaged terms is needed in semi-Lagrangian semi-implicit time-stepping schemes to help eliminate computational noise, especially when orographic forcing is present and at large Courant numbers (e.g., Rivest et al. 1994). In CSLAM-NH, no off-centering was needed to attain the numerical stability in the solver for the test cases presented here.

### *d. Conservative and consistent flux-form equations*

As noted by Lauritzen et al. (2006) and demonstrated in Wong et al. (2013) and Wong et al. (2014), when a numerical scheme different from the one used to evaluate the continuity equation is used to transport scalar variables, consistency in the scalar mass conservation equation is no longer guaranteed. The problem of numerical consistency in cell-integrated semi-Lagrangian schemes is resolved through the use of a new flux-form CISL continuity equation introduced in Wong et al. (2013) for the shallow-water equations and tested for a 2D nonhydrostatic atmosphere without topography (Wong et al. 2014). The new flux-form CISL continuity equation allows for a straightforward implementation of a CISL scalar transport scheme that ensures numerical consistency. Here, we further test the proposed formulation based on the CSLAM transport scheme for 2D idealized cases over mountains.

The potential temperature, continuity, and scalar-mass conservation equations are all solved consistently using the same numerical scheme presented in Wong et al. (2014):

$$\hat{\Theta}_m^{n+1} = \Theta_{m,\mathrm{exp}}^{n+1} + \frac{\Delta t}{2}\overline{[\nabla_{\mathrm{eul}} \cdot (\mathbf{v}'^n \hat{\Theta}_m^n)]}\frac{\delta A^*}{\Delta A} + \Delta t F_{\Theta_m}^n \frac{\delta A^*}{\Delta A} \tag{11a}$$

and

$$\tilde{\Theta}_m^{n+1} = \hat{\Theta}_m^{n+1} - \frac{\Delta t}{2}[\nabla_{\mathrm{eul}} \cdot (\mathbf{v}'^{n+1}\hat{\Theta}_m^{n+1})]. \tag{11b}$$

The flux divergence in terms of a corrective velocity $\mathbf{v}'$ in the semi-implicit correction term is defined as

$$\nabla_{\mathrm{eul}} \cdot (\Theta_m \mathbf{v}') = \frac{1}{\Delta x}[\overline{\Theta_m}^x(u_r - \mathcal{F}_r/\Delta\zeta) - \overline{\Theta_m}^x(u_l - \mathcal{F}_l/\Delta\zeta)] + \frac{1}{\Delta\zeta}[\overline{\Theta_m}^\zeta(\omega_t - \mathcal{F}_l/\Delta x) - \overline{\Theta_m}^\zeta(\omega_b - \mathcal{F}/\Delta x)],$$

where $\mathcal{F} = \mathcal{F}(u, \omega)$ are Lagrangian flux areas, computed as in Wong et al. (2014). The velocities $u_r$, $u_l$, $\omega_t$, and $\omega_b$ are staggered velocities at the cell faces.

In the semi-implicit flux-form equation, instead of linearizing around a mean reference state, we utilize $\hat{\Theta}_m^{n+1}$ using the CSLAM transport scheme to ensure consistency of the semi-implicit correction term among all the scalar flux-form equations. Included in this CSLAM computation are all the terms to be integrated over the departure cell: the explicit conservative CSLAM solution ($\Theta_{m,\mathrm{exp}}^{n+1}$), a predictor-corrector term (the flux divergence term at time level $n$), explicit diffusion, and diabatic tendency (the latter two are combined in $F_{\Theta_m}$). The diabatic tendencies are approximated using values at the previous time level. The resulting approximation $\hat{\Theta}_m^{n+1}$ in (11a) is then used in (11b). The solution from (11b) is the solution from the

dynamics, and prior to any adjustment to saturation by a moist microphysics scheme.

Consistent formulations of the continuity equation and scalar mass conservation equations are straightforwardly discretized as

$$\hat{\phi}^{n+1} = \phi_{\text{exp}}^{n+1} + \frac{\Delta t}{2}\overline{[\nabla_{\text{eul}} \cdot (\mathbf{v}'^{n}\hat{\phi}^{n})]}^{\delta A^*}_{\Delta A} + \Delta t F_{\phi}^{n}\frac{\delta A^*}{\Delta A}, \tag{12a}$$

and

$$\tilde{\phi}^{n+1} = \hat{\phi}^{n+1} - \frac{\Delta t}{2}[\nabla_{\text{eul}} \cdot (\mathbf{v}'^{n+1}\hat{\phi}^{n+1})], \tag{12b}$$

where $\phi = \tilde{\rho}_d$ or $Q_j$. Similar to (11a), (12a) combines the advected quantities in the explicit solution using the CSLAM scheme, the predictor-corrector flux divergence term, diffusion, and diabatic tendencies from the previous time level. The solution of the velocities at the new time level is used to compute the flux divergence in (12b).

### e. Helmholtz equation

By eliminating $\mathbf{v}'^{n+1}$ in the potential temperature equation in (11b) using the horizontal and vertical momentum equations, we form the Helmholtz equation:

$$\tilde{\Theta}_m'^{n+1} + \frac{\Delta t}{2}\langle \delta_x(\text{PG}_U\overline{\hat{\Theta}_m^{n+1}}^{x}) + \delta_\zeta\{[\zeta_x\overline{\overline{\text{PG}_U}^{x}}^{\zeta} + \zeta_z(1+\mu\Delta t)^{-1}\text{PG}_W]\overline{\hat{\Theta}_m^{n+1}}^{\zeta}\}\rangle$$
$$= \hat{\Theta}_m'^{n+1} - \frac{\Delta t}{2}[\delta_x(R_U\overline{\hat{\Theta}_m^{n+1}}^{x}) + \delta_\zeta(R_\Omega\overline{\hat{\Theta}_m^{n+1}}^{\zeta})], \tag{13}$$

where $\text{PG}_U$ and $\text{PG}_W$ are, as defined earlier, the implicit pressure-gradient terms expressed as functions of $\tilde{\Theta}_m^{n+1}$. All the terms on the rhs of (13) are precomputed at the beginning of each time step, and the implicit buoyancy term in $R_\Omega$ is updated at each iteration of the Helmholtz equation solver (described next).

### f. Iterative centered-implicit time-stepping scheme

The compressible Euler equations permit fast horizontally and vertically propagating acoustic and gravity waves. To alleviate the time-step limit due to acoustic waves, in the previous version of CSLAM-NH (Wong et al. 2014), an implicit time-stepping scheme was used to solve the pressure-gradient and mass-divergence terms. The remaining buoyancy terms were evaluated explicitly using a two time-level extrapolation scheme. The semi-implicit time integration scheme allowed the use of time steps much larger than those allowed in a classical explicit scheme, which would otherwise have been restricted by the speed of sound. The buoyancy terms responsible for gravity waves, however, imposed a restriction to the maximum stable time step.

Instead of evaluating the gravity wave terms explicitly using time extrapolation, we use an iterative approach for a more accurate and implicit treatment of these terms. The solution procedure can be summarized in two main components as follows. First, the departure cell areas are approximated using backward trajectories from the arrival gridcell vertices. The forcing terms ($R_U$, $R_\Omega$) and the explicit departure cell-averaged potential temperature, $\hat{\Theta}_m^{n+1}$ [using (11a)] are evaluated and form the rhs of the Helmholtz equation in (13). The implicit buoyancy term $B_W$ in $R_\Omega$ is evaluated at time level $n$ as an initial estimate. The explicit departure cell-averaged density $\hat{\rho}_d^{n+1}$ [using (12a)] is also precomputed. The second component involves solving the linear Helmholtz equation for $\tilde{\Theta}_m'^{n+1}$; here we use a conjugate gradient residual solver (Skamarock et al. 1997). The solution $\tilde{\Theta}_m'^{n+1}$ is then back substituted into the momentum equations in (7) and (10) to get $u^{n+1}$ and $\omega^{n+1}$, respectively. Finally, the implicit buoyancy term $B_W$ in (9) in $R_\Omega$ is updated using (i) $\tilde{\rho}_m'^{n+1}$ by evaluating (12b) and (ii) $\pi'^{n+1}$ directly from $\tilde{\Theta}_m'^{n+1}$ using the equation of state $\pi \equiv (R_d\Theta_m/p_0)^{R/c_v}$. At the end of the second component, the trajectories and forcing terms (first component of the procedure) are recomputed using the latest solution of $u^{n+1}$ and $\omega^{n+1}$.

Depending on the test case, two to four iterations of each component are performed. For the nonlinear flow tests, iterating more than twice did not further improve the maximum stable time step size. For the linear cases, the maximum time step can be further increased by performing more iterations (iterating more than four times does not further improve stability). At each iteration, the Helmholtz solver converges progressively faster (since the latest estimate of $\tilde{\Theta}_m'^{n+1}$ is used as the starting point). The iterative scheme is used for advancing the dry dynamics; after which, tracers are advected using (12b) and the moist physics are called (once at each time step).

The use of an iterative centered-implicit scheme is found to substantially increase the stable time step size in CSLAM-NH at the expense of solving the Helmholtz equation more than once per time step. To demonstrate

this behavior, we conduct the gravity wave test originally proposed in Skamarock and Klemp (1994), using CSLAM-NH as was done in Wong et al. (2014) with a grid spacing of $\Delta x = \Delta z = 1$ km and an imposed mean wind $\overline{U} = 20\,\mathrm{m\,s^{-1}}$. Wong et al. (2014) used an explicit treatment of the buoyancy terms and found that the maximum stable time step was restricted to $\Delta t = 38$ s [at a nominal Courant number (Cr) of 0.76]. In the current version of the iterative centered-implicit CSLAM-NH, we have found that for the same simulation, the maximum stable time step increased to 100 s, roughly by a factor of 2.6 (Cr = 2). For comparison, the maximum stable time step for an Eulerian split-explicit third-order Runge–Kutta time stepping scheme was 60 s (Cr = 1.2) (Wong et al. 2014).

Similar iterative approaches were found to improve numerical stability in other semi-Lagrangian solvers. In the Canadian Global Environmental Multiscale (GEM) model, Côté et al. (1998) discretize the governing equations in a fully implicit manner and use an iterative procedure to avoid solving a nonlinear Helmholtz equation. This procedure is also implemented in Melvin et al. (2010) for the vertical-slice nonhydrostatic solver using the Semi-Lagrangian Inherently Conserving and Efficient (SLICE) transport scheme. An alternative predictor-corrector (thus, also iterative) approach was tested in the European Centre for Medium-Range Weather Forecasts (ECMWF) Integrated Forecast System (IFS) model by Cullen (2001). In that study, a positive improvement in accuracy was noticeable only when the advective velocities, in addition to the buoyancy terms, were iterated. Using an idealized analysis of acoustic modes in a 1D nonhydrostatic vertical column, Cordero et al. (2005) demonstrated the impact of using time-extrapolated and -interpolated trajectory computations on the numerical stability of a semi-Lagrangian centered-semi-implicit scheme. When extrapolation and large time steps were used for the trajectories, the vertical structure of the acoustic modes were found to be distorted (with spurious zeros forming with time). The time-interpolation scheme on the other hand was found to be stable in all cases. The idealized analysis by Cordero et al. (2005) supports the findings in Cullen (2001) and the method used in Côté et al. (1998), with a recommendation for time-interpolated trajectory computations (e.g., by repeating the first component of the CSLAM-NH solution procedure).

The disadvantage of the present approach is that the linear Helmholtz equation for potential temperature $\Theta_m$ is solved a number of times with the buoyancy terms updated at the end of each iteration. However, the increased stability will allow a larger time step to be used and can help offset the added computational expense of solving the dry dynamics (calculated once at each time step). After the dry dynamics, the solver then advects passive tracers (once at each time step). With a larger time-step size, the total number of times tracers are advected during the entire simulation is reduced. Therefore, the overall execution time spent on scalar transport is also reduced. This reduction may have a significant impact on computational time, especially when the number of tracers used in chemistry applications is large.

### g. Boundary conditions

Periodic-in-$x$ and free-slip top and bottom boundary conditions are applied in all our tests. The vertical velocities at the top and bottom boundaries are set to $\omega = 0$, and ensures no normal flux through them. The boundary conditions are implemented by extrapolating $\Theta_m$, $\rho_d$, and $u$ into the boundary.

### h. Implicit Rayleigh damping

To prevent the reflection of vertically propagating gravity waves along the rigid model top, a damping term, $-\mu w$, is added in the vertical momentum equation based on the scheme proposed in Klemp et al. (2008) and implemented in Melvin et al. (2010). The damping profile $\mu(z)$ proposed by Klemp and Lilly (1978) is used:

$$\mu(z) = \begin{cases} \mu_{\max} \sin^2\left(\dfrac{\pi}{2}\dfrac{z - z_d}{z_t - z_d}\right) & \text{if} \quad z > z_d, \\ 0 & \text{if} \quad z \le z_d. \end{cases}$$

The profile is characterized by a gradual increase of viscosity with height, which is desirable to prevent any reflections that would otherwise occur from a sharp increase in viscosity. The damping layer starts from a user-specified height $z_d$ and extends to the top of the domain $z_t$. The depth of the damping layer is typically chosen to be about 1.5 to 2 times of the vertical wavelength ($\lambda_z = 2\pi\overline{U}/N$). The values of $\mu_{\max}$ are specified for each test case, and are chosen to be $0.05\,\mathrm{s^{-1}}$ for nonhydrostatic cases and $0.1\,\mathrm{s^{-1}}$ for hydrostatic cases. These values are estimated using the analysis from Klemp et al. (2008), where the authors experimented with a range of $\mu_{\max}$ and analyzed the reflection properties of this implicit Rayleigh damping layer. Based on their results of the reflection coefficient of the damping layer, we have chosen the $\mu_{\max}$ values based on a value of their nondimensional $\beta_w (= \mu_{\max}/kU) = 5$ and 50 for the nonhydrostatic and

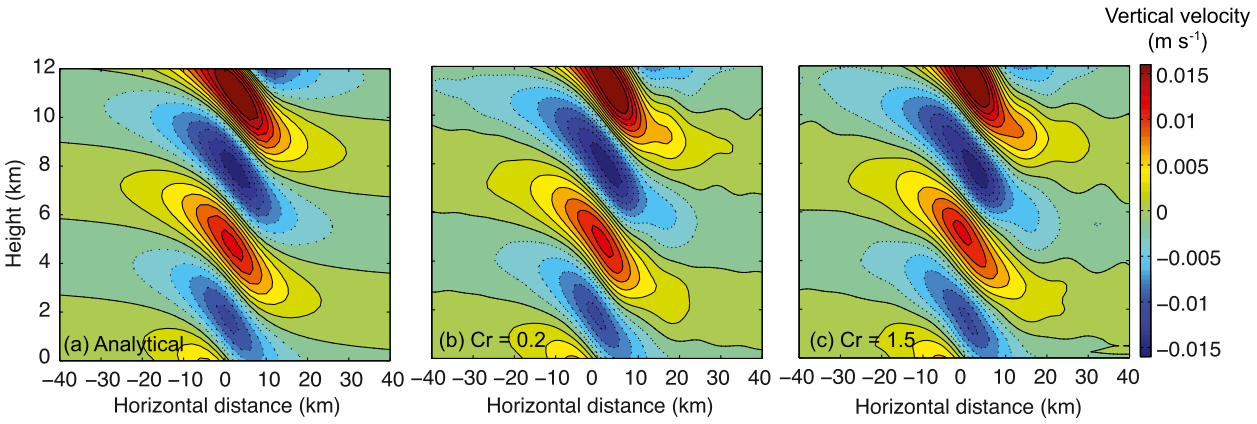


FIG. 2. Linear hydrostatic wave ($U/Na = 0.1$) for a low wide mountain showing vertical velocity $w$ ($\mathrm{m\,s^{-1}}$) obtained (a) analytically (following Smith 1980), (b) from CSLAM-NH after $T = 18$ h using $\Delta t = 20$ s (Cr = 0.2), and (c) $\Delta t = 150$ s (Cr = 1.5). The contour interval is $2 \times 10^{-3}\ \mathrm{m\,s^{-1}}$. Mean wind is from left to right.

hydrostatic cases, respectively. The scheme they proposed is slightly different from the one applied here; in particular, they proposed implementing the damping term as an adjustment step. The adjustment step approach includes an extra damping term that resembles vertical diffusion, in addition to the effect of a damping term $-\mu w$ added directly in the vertical momentum equation. For smaller (nonhydrostatic) horizontal scales, however, the effect of the damping term dominates and there is little difference between the two approaches.

## 3. Idealized test cases: Results

### *a. Linear mountain waves over bell-shaped mountain*

To test the response of the nonhydrostatic solver to orographic forcing, two adiabatic linear mountain-wave simulations are conducted first. Both cases assume a simple hill profile $h(x)$ of a witch-of-Agnesi curve, defined as

$$h(x) = \frac{h_m a^2}{x^2 + a^2},$$

with a small amplitude $h_m = 10$ m but different half-widths, $a$. Gravity waves generated by flow moving over a wide hill under conditions where $\overline{U}/Na \ll 1$ are approximately hydrostatic and are vertically propagating (Smith 1979). We simulate flow with a constant upstream wind speed $\overline{U} = 10\ \mathrm{m\,s^{-1}}$, with an initial stratification of $N^2 \approx 1 \times 10^{-4}\ \mathrm{s^{-2}}$. The mountain half-width is set at $a = 10$ km to give $\overline{U}/Na = 0.1$, such that nonhydrostatic effects are small for this broad low hill. The physical domain is 120 km wide and 20 km deep. The simulation is run for $t = 18$ h to ensure the solution has reached steady state and is not affected by any reflected waves from the model top. The numerical domain has dimensions 120 × 80 ($\Delta x = 1$ km and $\Delta z = 250$ m). A Rayleigh damping layer ($\mu_{\max} = 0.1\ \mathrm{s^{-1}}$) is implemented in the top 10 km of the domain (approximately 1.5 times the vertical wavelength, $\lambda_z = 2\pi\overline{U}/N = 6.28$ km).

Results from simulations using a small Courant number Cr = 0.2 and large Cr = 1.5, as well as the linear analytic solution [based on Smith (1980)] are shown in Fig. 2. An upstream tilt of the phase lines is observed, corresponding to energy originating from the ground (the mountain) and propagating upward. As expected, the amplitude of the vertical velocity also increases with height ($\propto \rho^{-1/2}$), corresponding to the effect of wave amplification due to decreasing density at higher altitudes. The slight downstream tilt of the wave pattern with height is due to weak nonhydrostatic influences and is also observed in other nonhydrostatic models for the same test case (e.g., Melvin et al. 2010). The solutions compare well with the analytic solution.

For a narrower mountain, the mountain waves are now nonhydrostatic. These waves are highly dispersive, with shorter horizontal scales propagating farther downstream with height, and scales less than $2\pi\overline{U}/N$ becoming evanescent. To simulate such a flow, the half-width $a$ of the mountain is reduced to 2 km. The impinging flow remains at $\overline{U} = 10\ \mathrm{m\,s^{-1}}$ ($\overline{U}/Na = 0.5$). The domain is 144 km wide and 25 km deep. The numerical domain has dimensions 360 × 100 grid cells ($\Delta x = 400$ m and $\Delta z = 250$ m). The Rayleigh damping layer is applied to the top 13 km of the domain (twice the length of $\lambda_z$) with $\mu_{\max} = 0.05\ \mathrm{s^{-1}}$.

Results from CSLAM-NH for two different time step sizes (Cr = 0.125 and Cr = 1.5), and the linear analytical

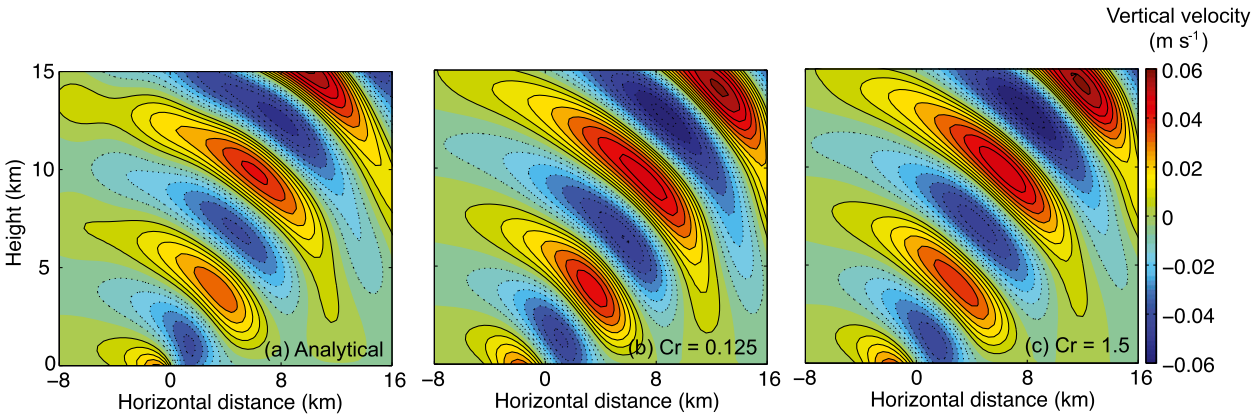


FIG. 3. Linear nonhydrostatic wave ($U/Na = 0.5$) for a narrow mountain showing vertical velocity $w$ ($\mathrm{m\,s^{-1}}$) obtained (a) analytically (following Smith 1980), (b) from CSLAM-NH after $T = 9000\,\mathrm{s}$ using $\Delta t = 5\,\mathrm{s}$ (Cr = 0.125), and (c) $\Delta t = 60\,\mathrm{s}$ (Cr = 1.5). The contour interval is $6 \times 10^{-3}\,\mathrm{m\,s^{-1}}$. Mean wind is from left to right.

solution [based on Smith (1980)] are shown in Fig. 3. As expected, far away and downstream of the mountain, the solutions exhibit a more pronounced downstream tilt of the phase from the nonhydrostatic component of the waves. The results compare well with the analytic solution and other solutions presented in the literature (e.g., Klemp et al. 2008; Xue et al. 2000; Melvin et al. 2010).

### b. *Schär mountain wave*

A more challenging test case is that proposed in Schär et al. (2002) of dry flow past an idealized topography. The topography prescribed includes a large-scale bell-shaped mountain with small-scale features of perturbation wavelength $\lambda$,

$$h(x) = h_m \exp\left[-\left(\frac{x - x_c}{a}\right)^2\right] \cos^2\left[\frac{\pi(x - x_c)}{\lambda}\right],$$

where $h_m = 250\,\mathrm{m}$ is the peak magnitude, $a = 5\,\mathrm{km}$ is the half-width, and $\lambda = 4\,\mathrm{km}$. The domain depth is 19.5 km, with a horizontal grid spacing of $\Delta x = 500\,\mathrm{m}$ and vertical grid spacing of 300 m. A reference temperature of 288 K and pressure of 100 kPa are used. The initial upstream wind profile is constant at $10\,\mathrm{m\,s^{-1}}$. An initial constant stratification $N = 0.01\,\mathrm{s^{-1}}$ is used. No explicit diffusion is applied. The numerical setup follows that of Schär et al. (2002), except for the horizontal domain size, which is increased from 200 to 400 km for the periodic lateral boundary conditions. A Rayleigh damping layer in the top 9.5 km is applied, as in original test case (with $\mu_{\max} = 0.15\,\mathrm{s^{-1}}$).

To reduce the impact of the small-scale topography features on the vertical coordinates at increasing heights, the basic terrain-following height coordinate (Gal-Chen and Somerville 1975) is modified by incorporating a smoothing function as proposed in Klemp (2011). The formulation of the smoothed terrain-following height coordinate gradually decreases the impact of the small-scale terrain features with increasing height. Figure 4 shows the linear analytical solutions and CSLAM-NH solutions of the vertical velocity at simulation time $T = 5\,\mathrm{h}$ using a time step size of 8 and 32 s (only partial domain is shown), comparing well to those in Schär et al. (2002) as well as those in Melvin et al. (2010).

### c. *Downslope windstorm*

To test the nonhydrostatic solver in a highly nonlinear flow, a simulation of the famous downslope windstorm that occurred on 11 January 1972 in Boulder, Colorado (Lilly 1978), is conducted. Strong surface winds, gusting to $55\,\mathrm{m\,s^{-1}}$, were observed in Boulder on that day. The windstorm has been a long-standing case for theory development and numerical model verification (e.g., Klemp and Lilly 1978; Peltier and Clark 1979; Durran 1986). More recently, Doyle et al. (2000) carried out a model intercomparison study of 11 different high-resolution models to assess their ability in numerically simulating the wave-breaking process of this windstorm. Prior to Doyle et al. (2000), smoothed soundings were used to initialize the models; here, we use the same 1200 UTC 11 January 1972 Grand Junction, Colorado, sounding as in Doyle et al. (2000), where they showed that a more realistic simulation of the windstorm was generated.

The numerical setup is based on Doyle et al. (2000). The mountain half-width is 10 km with a height of 2 km. The domain is 240 km wide and 25 km deep. The numerical domain dimensions are 240 × 125 grid cells ($\Delta x = 1\,\mathrm{km}$ and $\Delta z = 200\,\mathrm{m}$). The time step sizes used

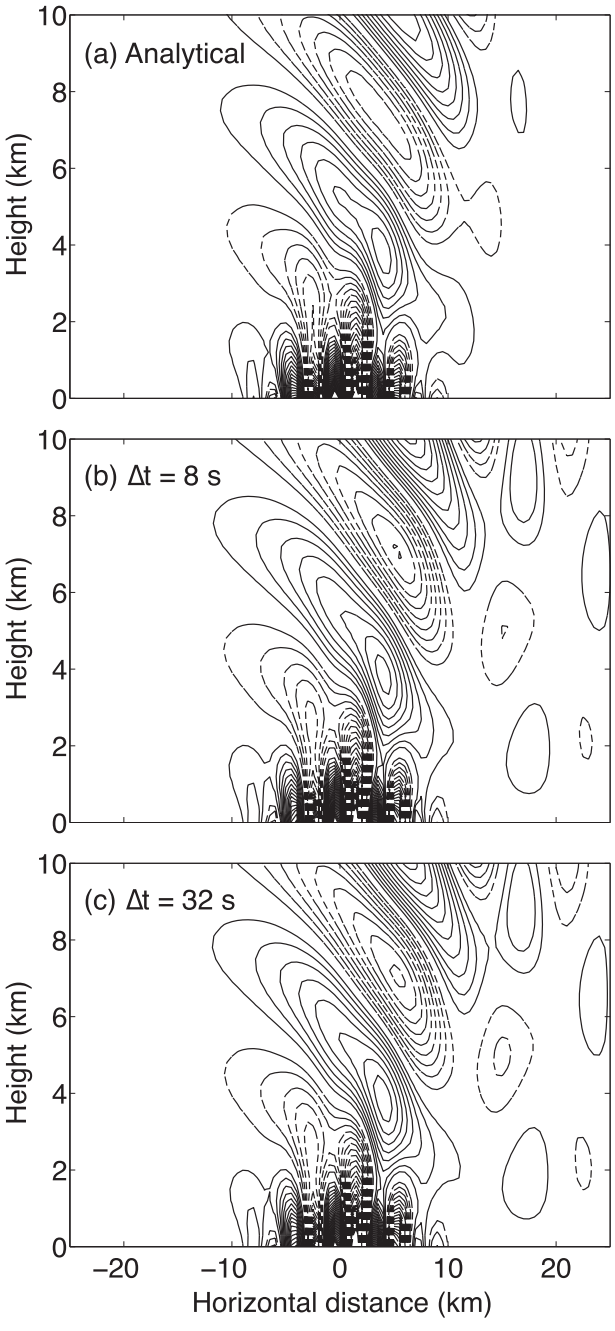


FIG. 4. Vertical velocity $w$ ($\mathrm{m\,s^{-1}}$) for the Schär mountain wave test obtained (a) analytically [following a procedure similar to Smith (1980)], (b) from CSLAM-NH after $T = 5$ h using $\Delta t = 8$ s, and (c) $\Delta t = 32$ s. The contour interval is 0.05 $\mathrm{m\,s^{-1}}$. Solid (dashed) lines indicate positive (negative) velocities. Mean wind is from left to right.

in Doyle et al. (2000) ranged from 1 to 12 s [the largest time step size of 12 s was run using the model in Durran and Klemp (1983), which uses a time-splitting scheme with a small time step of 3 s]. To compare the results with these models, a similar time step size of 10 s is used in CSLAM-NH. A Rayleigh damping layer ($\mu_{\max} = 0.05\,\mathrm{s^{-1}}$) is applied only in the top 7 km of the domain ($18 \le z \le 25$ km) to prevent the damping of the physically significant wave breaking in the lower stratosphere. A fourth-order horizontal smoothing filter is applied and evaluated at time level $n$ with a coefficient $K_D = 1 \times 10^9\,\mathrm{m^4\,s^{-1}}$, which smooths out any small-scale variations in the velocities and potential temperature and helps maintain numerical stability in the model. Unlike most of the models in Doyle et al. (2000), no turbulence parameterization or any other explicit diffusion was used; turbulent dissipation is solely dependent on the hyperviscosity applied and any inherent numerical dissipation associated with the model discretization.

In the results presented within Doyle et al. (2000), all models produced significant strengthening of the winds on the lee of the mountain and wave breaking in the upper troposphere and stratosphere at time 3 h. Despite using identical initial conditions, however, significant differences were found among the model results due to differences in the model formulations (e.g., spatial and temporal discretizations, type of explicit diffusion used, etc.), as well as the nonlinearity of the flow.

The CSLAM-NH results at 3 h are presented in Fig. 5. The wave-breaking regions in CSLAM-NH can be identified as the adiabatic (well mixed) regions (Fig. 5a) and highly turbulent areas (Richardson number, $R_i < 0.25$) [Fig. 5c, where to be consistent with Doyle et al. (2000), the Richardson number $\mathrm{sgn}(R_i)|R_i|^{0.5}$ is plotted]. The Richardson number used in Fig. 5c is the bulk Richardson number (dry):

$$R_i = \frac{g/\theta(\Delta\theta/\Delta z)}{(\Delta u/\Delta z)^2}.$$

For locally statically stable air ($R_i > 0$), the critical Richardson number at which wind shear is strong enough to sustain turbulence and overcome the damping by negative buoyancy is 0.25. The wave-breaking regions appear to be in the vicinity of $12 \le z \le 16$ km and $17 \le z \le 20$ km, comparable to the results in the intercomparison study. An initial critical level at $z = 21$ km (where $U = 0$) is also found to be damping in the CSLAM-NH model simulation, and traps the vertically propagating gravity waves. The damping effect is evident in the smooth isentropes and lack of turbulence (large $R_i$, not contoured) above that height.

The lateral position of the hydraulic jumps at 3 h varied among the models given in Doyle et al. (2000), with several occurring over the lee slope and others farther downstream. The associated maximum lee slope winds from the 11 models were found to range

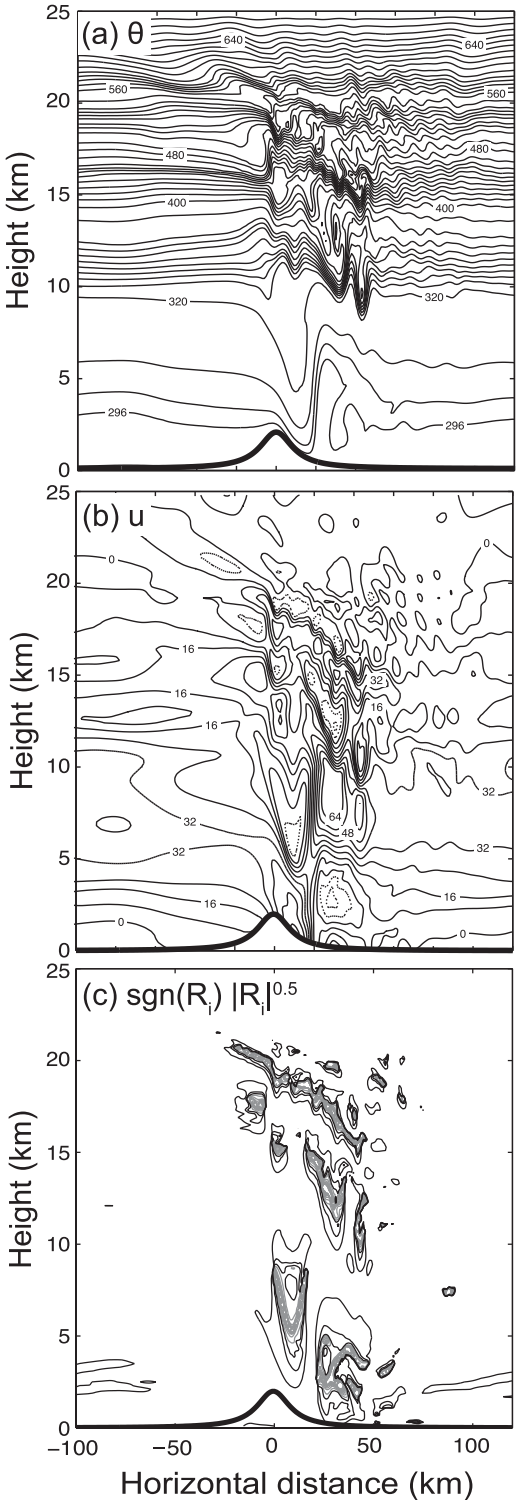


FIG. 5. CSLAM-NH simulation for the 1972 Boulder windstorm case (a) potential temperature $\theta$ (K) (with a contour interval of 8 K), (b) horizontal velocity $U$ (m s$^{-1}$) (with a contour interval of 8 m s$^{-1}$), and (c) Richardson number $\mathrm{sgn}(R_i)|R_i|^{0.5}$ [$-5 \le R_i \le 1$ are plotted with contour interval of 0.5, following Doyle et al. (2000); the gray shaded area shows negative values] at $T = 3$ h using a time step $\Delta t = 10$ s.

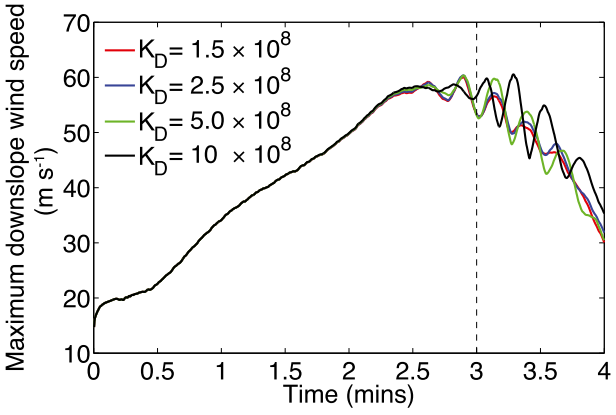


FIG. 6. Time series of the simulated maximum CSLAM-NH downslope wind speeds (m s$^{-1}$) for the 1972 Boulder windstorm case using different horizontal smoothing coefficients, $K_D$(m$^4$ s$^{-1}$).

from 43 to 86 m s$^{-1}$. In CSLAM-NH, the hydraulic jump feature is found on the lee slope, and the simulated maximum downslope wind speed at the surface (lowest model level) is located at 10.5 km downstream from the mountain crest at 56.6 m s$^{-1}$ (Fig. 5b). Flow features aloft such as the flow reversal at $5 \le z \le 10$ km that was present in many of the models in Doyle et al. (2000), are also present in the CSLAM-NH results. This weakening of the winds above the hydraulic jump was also observed in the aircraft flight data analysis [see, e.g., Fig. 2b in Doyle et al. (2000)].

The hyperviscosity coefficients used by the models in the model intercomparison study ranged from $1.1 \times 10^8$ to $5.0 \times 10^9$ m$^4$ s$^{-1}$. Time series of simulated maximum downslope wind speeds using different diffusion coefficients in CSLAM-NH are given in Fig. 6. Results from varying the horizontal smoothing coefficient from $1.5 \times 10^8$ to $1 \times 10^9$ m$^4$ s$^{-1}$ show a slight variation in the simulated maximum downslope wind speed, with values at 3 h ranging from 53.1 to 56.6 m s$^{-1}$. The impact of using different magnitudes of horizontal smoothing is apparent once the waves begin to break, giving a maximum range of predicted downslope wind speeds of approximately 12 m s$^{-1}$. The general trend of the downslope windstorm development, however, is similar with maximum surface winds of the simulation occurring at around 3 h, with weakening thereafter due to the limited horizontal extent of the domain and periodic lateral boundaries.

The maximum stable time step in CSLAM-NH for this wave-breaking case is 20 s (when $K_D = 5.0 \times 10^9$ m$^4$ s$^{-1}$ is applied). With a time step larger than 20 s, the errors of the linear trajectory approximations become large enough that the departure cells self-intersect as illustrated in Fig. 7. In this case, the flow is characterized by

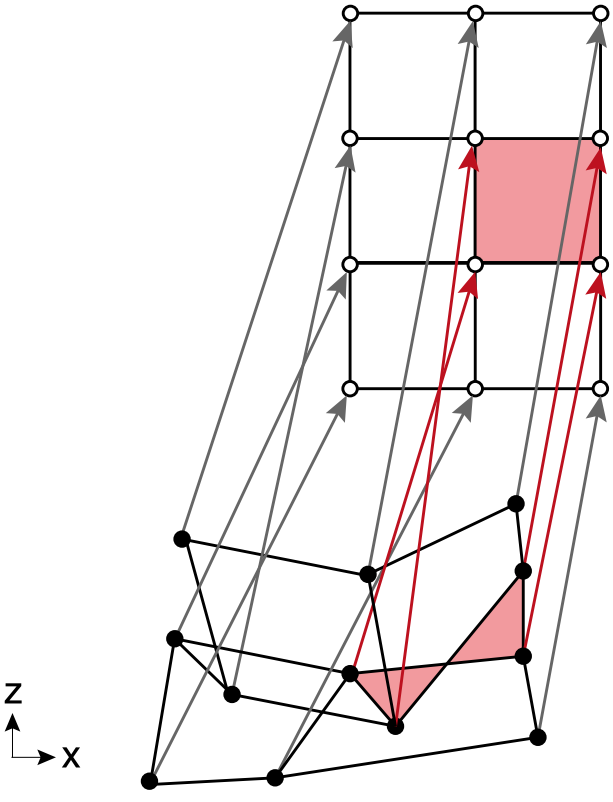


FIG. 7. A self-intersecting departure cell (highlighted in red with vertices marked by black circles) in CSLAM-NH when a large time step size of 25 s is used for the strongly sheared flow in the 1972 Boulder downslope windstorm case. Black circles indicate departure gridcell vertices and white circles the Eulerian arrival gridcell vertices. Arrows symbolize the computed backward-in-time trajectories. Trajectories and the arrival grid cell associated with the self-intersecting departure cell are highlighted in red.

a strong horizontal shear of the vertical wind speeds as well as large vertical Courant number, $\mathrm{Cr}_z \approx 3$ (not shown). Higher-order cell-edge approximations have been explored by Ullrich et al. (2013), and may help alleviate the time step limit by increasing the accuracy of the area integration. Overall, CSLAM-NH is able to generate comparable results to the other models, and at a maximum time step size that is roughly double those used in Doyle et al. (2000).

### d. *Moist flow over a mountain in a nearly neutral environment*

The nonhydrostatic solver is tested for another nonlinear flow, but in this case, we also include the effects from moist processes. A simulation of saturated flow over a mountain in an initially nearly neutral environment is conducted. This test case also demonstrates the ability of the solver in producing realistic orographic precipitation. The simulation is based on the test cases presented in Miglietta and Rotunno (2005). Moisture in the atmosphere is an important factor in modifying flow over topography. Durran and Klemp (1983) studied the influence of moisture on mountain waves using numerical simulations. In both a linear mountain-wave test and a downslope-windstorm test, they found that the inclusion of upstream moisture can greatly reduce the amplitude of these waves relative to their dry analogs. As the mountain enhances lifting of the moist flow over the windward side, condensation commonly occurs, leading to clouds and precipitation. The downstream evaporation of these clouds and precipitation can reduce the static stability at these altitudes, and the air can become desaturated on the lee side of the mountain due to rainout processes and adiabatic warming in the descent.

For a nearly neutral flow, Miglietta and Rotunno (2005) simulated the transition of saturated air upstream to unsaturated air downstream due to diabatic warming in the downward motion on the lee. The inverse Froude number $N_m h_m/U$ is near zero, indicating that the resistance due to gravity is minimal and the flow can freely translate over the mountain.

To include moisture effects when determining local static stability, Lalas and Einaudi (1974), and later verified by Durran and Klemp (1982), derived an expression for the moist Brunt–Väisälä frequency:

$$N_m^2 = g\Gamma\left(\frac{d\ln\theta}{dz} + \frac{L_v}{c_p T}\frac{dq_s}{dz}\right) - \frac{g}{1+q_w}\frac{dq_w}{dz}, \quad (14)$$

where $T$ is the absolute temperature, $q_s$ is the saturated water vapor mixing ratio, $q_w$ is the total water mixing ratio, and

$$\Gamma = \frac{1 + \dfrac{1}{q_s + \epsilon}\left.\dfrac{\partial q_s}{\partial \ln\theta}\right|_\pi}{1 + \dfrac{L_v}{c_p T}\left.\dfrac{\partial q_s}{\partial \ln\theta}\right|_\pi}, \quad (15)$$

is the ratio of the moist to dry adiabatic lapse rates. (All other variables are as defined previously.) More details on the generation of the saturated neutral sounding for a specific moist static stability $N_m$ and surface temperature are given in the appendix.

Miglietta and Rotunno (2005) used a small $N_m^2 = 3 \times 10^{-6}\ \mathrm{s}^{-2}$ to represent a nearly neutral troposphere due to the limitations of the single machine precision accuracy of their model. They found that using any smaller $N_m$ led to solutions that were apparently convectively unstable. The CSLAM-NH solver has machine double precision accuracy, so for

this moist neutral flow case, an initial $N_m = 0$ in the troposphere is applied. Simulations using a range of "small" $N_m^2 \sim 10^{-11}\,\mathrm{s}^{-2}$ in the initialization step show solutions similar to applying $N_m = 0$ and resemble those in Miglietta and Rotunno (2005) more than using their $N_m^2 = 3 \times 10^{-6}\,\mathrm{s}^{-2}$. An initial $N_m^2 = 4.84 \times 10^{-4}\,\mathrm{s}^{-2}$ is used for the isothermal stratosphere.

Two mountain cases with different heights, $h_m = 700$ m and 2 km, were chosen from Miglietta and Rotunno (2005) for their distinct differences in orographic distribution of moisture. Both test cases are run using the Witch-of-Agnesi curve with a half-width of 10 km. The same numerical domain that is 800 km wide and 20 km deep is used, and the grid dimensions are 400 × 80 grid cells ($\Delta x = 2$ km and $\Delta z = 250$ m). In both cases, a mean wind $\overline{U} = 10\,\mathrm{m\,s}^{-1}$ is applied. The atmosphere is initially saturated ($q_v \equiv q_s$) with constant cloud water mixing ratio $q_c = 0.05\,\mathrm{g\,kg}^{-1}$ set everywhere in the domain to prevent the atmosphere from becoming subsaturated due to the impulsive introduction of the mountain at initial time. The Rayleigh damping layer ($\mu_{\max} = 0.1\,\mathrm{s}^{-1}$) is applied in the top 5 km of the domain. Second-order filters in the horizontal and vertical directions are applied with coefficients 3000 and $3\,\mathrm{m}^2\,\mathrm{s}^{-1}$, respectively. The Prandtl number is 3. This configuration is the same as that in Miglietta and Rotunno (2005).

Both cases suggest a desaturation of the air downstream of the mountain with time. Miglietta and Rotunno (2005) noticed in their simulations that for intermediate mountain heights ($500 \le h_m \le 1500$ m) the unsaturated region downstream of the hill unexpectedly extends upstream as well. A later study by Keller et al. (2012) showed that this upstream extent of the subsaturated air is due to local adiabatic descent and warming caused by a transient upstream-propagating gravity wave, a fundamental feature of a two-layer two-dimensional atmosphere with topography introduced impulsively. The purpose of performing the test case as prescribed in Miglietta and Rotunno (2005) with a mountain 700 m high is to ensure that CSLAM-NH can generate comparable results to models used in the literature, such as that in Miglietta and Rotunno (2005), who used the Weather Research and Forecasting (WRF) Model (version 1.3).

Figure 8 shows the solution from CSLAM-NH [cf. Fig. 5d of Miglietta and Rotunno (2005)] using a time step size of 20 s. The white region indicates subsaturated air, as described previously. Although the upstream region of the subsaturated air in Miglietta and Rotunno (2005) extends farther upstream ($x = -100$ km) than that found using CSLAM-NH, the solution from CSLAM-NH compares very well with that obtained in Miglietta and Rotunno (2005). The maximum stable CSLAM-NH time step size is 50 s with two iterations

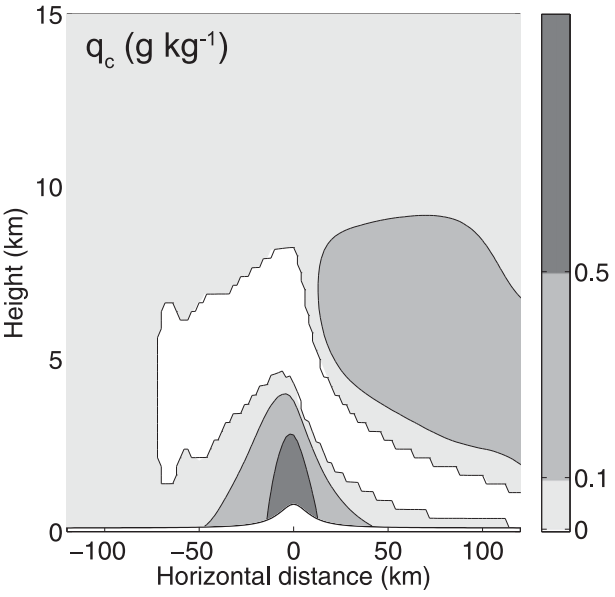


FIG. 8. CSLAM-NH cloud water mixing ratio (g kg$^{-1}$) at time 5 h from an initially saturated nearly neutral flow (with an initial $q_c = 0.05\,\mathrm{g\,kg}^{-1}$) over a 700-m hill. The white region above ground indicates subsaturated air ($q_c \equiv 0$).

of both components in the iterative centered-implicit scheme.

Figure 9a shows the CSLAM-NH cloud water mixing ratio at time 5 h 10 min (10 min after autoconversion of rain is permitted) of a simulation using $\Delta t = 20$ s for the large-amplitude mountain ($h_m = 2$ km) case [cf. black contours in Fig. 8a in Miglietta and Rotunno (2005)]. Similar to the results presented in Miglietta and Rotunno (2005), no upstream region of the subsaturated air is found. In addition, the formation of convective cells due to the reduction of local static stability downstream of the mountain is also detected in the CSLAM-NH simulation. The instability is found to be primarily associated with a hydraulic jump feature downwind. Figure 9b shows the rainwater mixing ratio for the same simulation time as in Fig. 9a.

Compared to the results in Miglietta and Rotunno (2005), CSLAM-NH indicates more rain spillover to the lee of the mountain [cf. gray contours in Fig. 8a in Miglietta and Rotunno (2005)]. Simulation of our case using an Eulerian split-explicit model similar to the one used in Miglietta and Rotunno (2005) shows virtually the same distributions of cloud water and rainwater as in the CSLAM-NH simulation (Fig. 9). The similarity of the CSLAM-NH solution to that of the second Eulerian model seems to suggest that the discrepancy is not specific to CSLAM-NH and may be related to certain aspects of the initialization procedure. Miglietta and Rotunno (2005) suggested that their simulations were

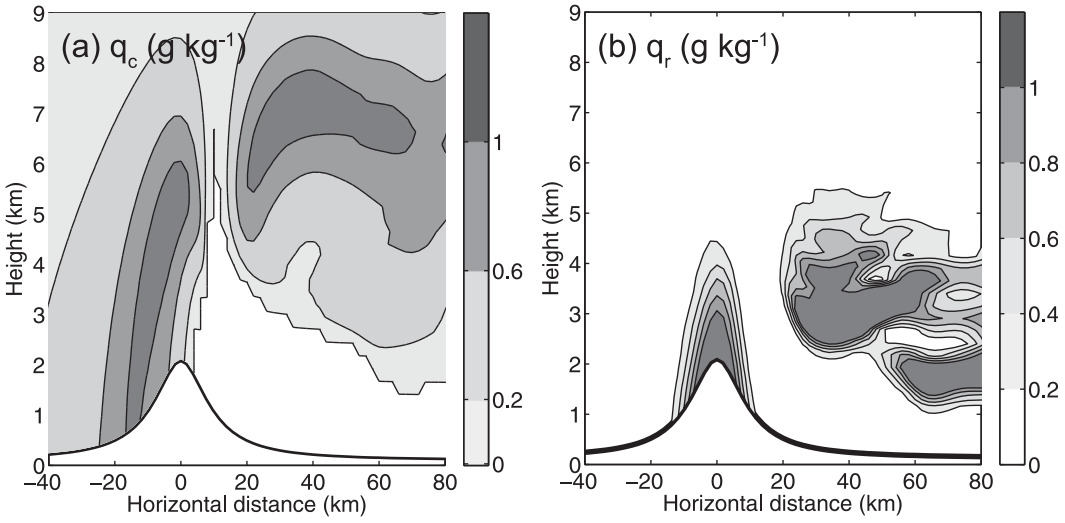


FIG. 9. (a) As in Fig. 8 but at time 5 h 10 min over a 2-km mountain. (b) CSLAM-NH rainwater mixing ratio $q_r$ (g kg$^{-1}$) at the same simulation time.

sensitive to small changes to $N_m \approx 0$. If there is a slight discrepancy between the value of $N_m$ specified in the initialization than that used in Miglietta and Rotunno (2005), the flow dynamics may be altered. In this situation, the greater amount of waterloading to the lee of the mountain could imply a lower effective terrain height ($N_m h_m/\overline{U}$) (i.e., lower stability and/or stronger winds), such that the advection of the hydrometeors happens at a faster time scale than the fallout of precipitation.

Using this moist neutral flow test, the computational performance of the serial CSLAM-NH is evaluated. The computational efficiency of the CSLAM-NH solver depends on two main components: the Helmholtz solver and the transport of the passive scalars. The current iterative Helmholtz solver allows for a larger time step size at the expense of solving the Helmholtz equation more than once. Compared to the noniterative scheme, which has a smaller maximum stable time step, the larger stable time step improves the overall efficiency by 43%, albeit the iterations and slower Helmholtz solver convergence.

In the current version of CSLAM-NH, the computational cost of the cell-integrated transport scheme is roughly double of that of an Eulerian comparison solver that uses a third-order Runge–Kutta split-explicit time-stepping scheme. For CSLAM-NH to be comparable in execution time to the Eulerian solver, the CSLAM-NH time step size needs to be roughly 5 times that of the Eulerian time step. The maximum stable CSLAM-NH time step size is found to be limited by self-intersecting departure cells. Special handling of the self-intersecting departure cells (such as artificially "uncoiling" these twisted cells) may help increase the stability of CSLAM-NH. We note that the performance of CSLAM-NH will likely compare very differently in a multiprocessor environment (discussed in the next section).

## 4. Summary

A nonhydrostatic atmospheric solver (CSLAM-NH) that uses a new discrete formulation of the semi-implicit continuity equation for cell-integrated semi-Lagrangian transport schemes is developed and further tested for flows over idealized orography. Here, the solver using the CSLAM transport scheme is tested against various idealized mountain-wave cases and exhibits accurate and stable behavior under the influence of a terrain-following height coordinate. An implicit Rayleigh damping layer is also implemented in this extended version of CSLAM-NH to help prevent unphysical reflection of vertically propagating gravity waves at the model top.

The new discrete semi-implicit continuity equation used in CSLAM-NH allows for a straightforward implementation of consistent flux-form equations for scalars in the model. Consistency in conservative scalar mass transport may prove to be important in longer NWP and climate simulations. The time integration of both the gravity and acoustic waves are handled implicitly in the solver using an iterative centered-implicit scheme. The iterative scheme allows for larger maximum stable time step sizes at the expense of solving the linear Helmholtz problem more than once.

In large climate and chemistry models, the computational cost associated with the parameterized physics and the transport of the many [$O(10^2)$] tracer species is likely to outweigh that associated with the dynamics.

The solution procedure for the dry dynamics is carried out once at each time step, whereas scalar transport is computed for hundreds of tracers. The larger time step sizes allowable by the iterative scheme in CSLAM-NH reduce the number of tracer advection steps per simulation, which may help compensate for the added expense.

In a parallel environment, the performance of CSLAM-NH will likely depend on the scalability of the CSLAM transport scheme, and the Helmholtz solver. Erath et al. (2012) implemented and optimized the CSLAM transport scheme to run in HOMME, one of the dynamical core options in the Community Atmosphere Model (CAM). The computational performance of using the CSLAM transport scheme was found to be much more efficient and scalable than the advection scheme in HOMME, which uses a three-stage second-order Runge–Kutta time-stepping scheme. Erath et al. (2012) found that the CSLAM transport scheme was able to outperform the scheme in HOMME, not because of fewer floating-point operations, but largely because the latter required much more (approximately 10 times) communication time than the CSLAM transport scheme when a large number of processors are used. Regarding efficient parallelizable Helmholtz solvers, Müller and Scheichl (2014) recently explored and compared several different approaches. The authors demonstrated that the geometric multigrid method they tested can be roughly 5–10 times faster than the algebraic multigrid methods and preconditioned conjugate gradient solvers that they have also tested, in a parallel environment. Since the Helmholtz equation in CSLAM-NH is formulated to be similar to those solved by traditional elliptic solvers, recent improved techniques such as those in Müller and Scheichl (2014) are also applicable when implementing CSLAM-NH for a parallel environment.

Four idealized test cases available from the literature were used to verify the stability and accuracy of the proposed solver over topography. Simulations of linear hydrostatic and nonhydrostatic mountain waves compared well with numerical solutions from the literature. The simulation of a highly nonlinear wave-breaking case of the 11 January 1972 Boulder windstorm highlighted the ability of the solver to handle highly sheared flow at large time steps. Because of the strong nonlinearity of the flow, the simulations from the models used in the intercomparison study of Doyle et al. (2000) varied in their finescale features. Although there is limited predictability of the precision of these features, all models, including CSLAM-NH (the simulation of which is presented here), showed similar main features of the windstorm, such as the locations of the wave-breaking regions and hydraulic jump downstream of the mountain. Finally, moist nearly neutral orographic flows based on Miglietta and Rotunno (2005) are tested. Two mountain profiles were used: a lower 700-m-tall mountain and a much higher 2-km mountain. For the lower mountain case, CSLAM-NH shows comparable results with those in Miglietta and Rotunno (2005), including downstream and upstream regions of subsaturated air. For the higher mountain case, there is more rain spillover to the lee side of the mountain as compared to the results presented in Miglietta and Rotunno (2005). However, similar solutions are found using another comparison Eulerian split-explicit model, which suggests that certain aspects (e.g., initialization) of the model other than model formulation may be causing the discrepancy, and that the discrepancy is not specific to CSLAM-NH.

In its current state of development, CSLAM-NH is a two-dimensional prototypical nonhydrostatic atmospheric solver in Cartesian geometry that has shown promising potential for weather and climate applications. Attractive features of this solver include the consistent formulation of the semi-implicit cell-integrated semi-Lagrangian continuity and scalar conservation equations, in conjunction with the inherently conservative multitracer CSLAM transport scheme. For the solver to be further implemented as a dynamical core in a full NWP and climate model, the Coriolis terms, which have been neglected thus far, should be incorporated back into the solver. The Coriolis terms were tested in a similar solver on the shallow-water system in Wong et al. (2013). In addition, the discretization will need to be extended to a sphere, and the CSLAM transport scheme implemented for three-dimensional transport.

*Acknowledgments.* The initial research of this work was done during the first author's visits to the National Center for Atmospheric Research through the Graduate Visitor Advanced Study Program. The authors thank Dr. James Doyle for providing the sounding data used in the initialization of the 11 January 1972 Boulder windstorm case. This research is funded by the Canadian Natural Science and Engineering Research Council via a Discovery Grant to the last author.

## APPENDIX

### Generation of a Moist Neutral Sounding

A few more specifics regarding the generation of the moist neutral sounding that supplements the derivation presented in Miglietta and Rotunno (2005) are given. Following the procedure in Miglietta and Rotunno (2005), to generate the initial sounding of

a specific $N_m$, a first-order ordinary differential equation is solved. To create the initial nearly neutral sounding, the first-order ordinary differential equation for potential temperature is solved iteratively based on a specified surface temperature (15°C) and reference pressure ($p_0 = 100\,\text{kPa}$). To be consistent with Miglietta and Rotunno (2005), the Wexler's formula for saturated vapor pressure (in hPa) is used:

$$e_s(T) = 6.11 \exp\left(17.67 \frac{T - 273.15\,\text{K}}{T - 29.65\,\text{K}}\right). \quad \text{(A1)}$$

The definition for $q_s = \epsilon e_s/(p - e_s)$, where $\epsilon = R_d/R_v$ is used to derive $\partial q_s/\partial \ln\theta|_\pi$ in (15). First, differentiating $q_s$ with respect to $\ln\theta$ at constant Exner function $\pi$ gives

$$\left.\frac{\partial q_s}{\partial \ln\theta}\right|_\pi = \frac{q_s}{e_s}\frac{p}{p - e_s}\left.\frac{\partial e_s}{\partial \ln\theta}\right|_\pi,$$

and differentiating (A1) (using $T = \pi\theta$) with respect to $\ln\theta$ at constant $\pi$ gives the following expression:

$$\left.\frac{\partial e_s}{\partial \ln\theta}\right|_\pi = e_s T \frac{17.67(243.5)}{(T - 29.65)^2}.$$

To find $\theta(z)$ for a specific $N_m$, (14) must be iterated to convergence ($10^{-12}$) at each pressure level (or height) since $q_s = q_s(\pi, \theta)$ and $\Gamma$ are also functions of the unknown. To get the pressure at each height, the hydrostatic equation is used:

$$\frac{\pi_{j+1} - \pi_j}{\Delta z} = -\frac{g}{c_p}\frac{\overline{1 + q_w}^z}{\overline{\theta_m}^z}.$$

For each model level $j$, the discrete form of the ODE solving for $\theta$ at height $z$ is

$$\ln\theta_{j+1} + \frac{\overline{L_v}^z}{c_p T}(q_{s,j+1} - q_{s,j}) - (q_{w,j+1} - q_{w,j})\overline{\left[\frac{1}{(1 + q_w)\Gamma}\right]}^z = \ln\theta_j + \frac{\overline{N_m^2}^z}{g\Gamma}(z_{j+1} - z_j).$$

[Note: Miglietta and Rotunno (2005) express this equation in terms of $(T, p)$.] Other aspects of the Kessler microphysics scheme also require modification. Following Miglietta and Rotunno (2005), no autoconversion from cloud water to rain is permitted in the first 5 h to allow for initial adjustment of the flow to the impulsive introduction of terrain. For a consistent definition of $q_s$ throughout the model, the production of cloud water due to saturation is also modified:

$$\left|\frac{dq_s}{dt}\right| = \frac{q_v - q_s}{1 + \frac{L_v}{c_p}\left.\left(\frac{\partial q_s}{\partial T}\right)\right|_p},$$

where, based on the Wexler's equation for $e_s$:

$$\left.\frac{\partial q_s}{\partial T}\right|_p = \frac{q_s p}{p - e_s}\frac{17.67(243.5)}{(T - 29.65)^2}.$$

## REFERENCES


Bonaventura, L., 2000: A semi-implicit semi-Lagrangian scheme using the height coordinate for a nonhydrostatic and fully elastic model of atmospheric flows. *J. Comput. Phys.,* **158,** 186–213, doi:10.1006/jcph.1999.6414.

Cordero, E., N. Wood, and A. Staniforth, 2005: Impact of semi-Lagrangian trajectories on the discrete normal modes of a non-hydrostatic vertical-column model. *Quart. J. Roy. Meteor. Soc.,* **131,** 93–108, doi:10.1256/qj.04/34.

Côté, J., S. Gravel, A. Méthot, A. Patoine, M. Roch, and A. Staniforth, 1998: The operational CMC-MRB global environmental multiscale (GEM) model. Part I: Design considerations and formulation. *Mon. Wea. Rev.,* **126,** 1373–1395, doi:10.1175/1520-0493(1998)126<1373:TOCMGE>2.0.CO;2.

Cullen, M. J. P., 2001: Alternative implementations of the semi-Lagrangian semi-implicit schemes in the ECMWF model. *Quart. J. Roy. Meteor. Soc.,* **127,** 2787–2802, doi:10.1002/qj.49712757814.

Doyle, J. D., and Coauthors, 2000: An intercomparison of model-predicted wave breaking for the 11 January 1972 Boulder windstorm. *Mon. Wea. Rev.,* **128,** 901–914, doi:10.1175/1520-0493(2000)128<0901:AIOMPW>2.0.CO;2.

Durran, D. R., 1986: Another look at downslope windstorms. Part I: The development of analogs to supercritical flow in an infinitely deep, continuously stratified fluid. *J. Atmos. Sci.,* **43,** 2527–2543, doi:10.1175/1520-0469(1986)043<2527:ALADWP>2.0.CO;2.

——, and J. B. Klemp, 1982: On the effects of moisture on the Brunt–Väisälä frequency. *J. Atmos. Sci.,* **39,** 2152–2158, doi:10.1175/1520-0469(1982)039<2152:OTEOMO>2.0.CO;2.

——, and ——, 1983: A compressible model for the simulation of moist mountain waves. *Mon. Wea. Rev.,* **111,** 2341–2361, doi:10.1175/1520-0493(1983)111<2341:ACMFTS>2.0.CO;2.

Erath, C., P. H. Lauritzen, J. H. Garcia, and H. M. Tufo, 2012: Integrating a scalable and efficient semi-Lagrangian multi-tracer transport scheme in HOMME. *Procedia Comput. Sci.,* **9,** 994–1003, doi:10.1016/j.procs.2012.04.106.

Gal-Chen, T., and R. Somerville, 1975: On the use of a coordinate transformation for the solution of the Navier-Stokes equations. *J. Comput. Phys.,* **17,** 209–228, doi:10.1016/0021-9991(75)90037-6.

Jöckel, P., R. von Kuhlmann, M. Lawrence, B. Steil, C. Brenninkmeijer, P. Crutzen, P. Rasch, and B. Eaton, 2001: On a fundamental problem in implementing flux-form advection schemes for tracer transport in 3-dimensional general circulation and chemistry transport models. *Quart. J. Roy. Meteor. Soc.,* **127,** 1035–1052, doi:10.1002/qj.49712757318.

Keller, T. L., R. Rotunno, M. Steiner, and R. D. Sharman, 2012: Upstream-propagating wave modes in moist and dry flow over topography. *J. Atmos. Sci.,* **69,** 3060–3076, doi:10.1175/JAS-D-12-06.1.

Klemp, J. B., 2011: A terrain-following coordinate with smoothed coordinate surfaces. *Mon. Wea. Rev.,* **139,** 2163–2169, doi:10.1175/MWR-D-10-05046.1.

——, and D. K. Lilly, 1978: Numerical simulation of hydrostatic mountain waves. *J. Atmos. Sci.,* **35,** 78–107, doi:10.1175/1520-0469(1978)035<0078:NSOHMW>2.0.CO;2.

——, W. C. Skamarock, and J. Dudhia, 2007: Conservative split-explicit time integration methods for the compressible nonhydrostatic equations. *Mon. Wea. Rev.,* **135,** 2897–2913, doi:10.1175/MWR3440.1.

——, J. Dudhia, and A. D. Hassiotis, 2008: An upper gravity-wave absorbing layer for NWP applications. *Mon. Wea. Rev.,* **136,** 3987–4004, doi:10.1175/2008MWR2596.1.

Lalas, D. P., and F. Einaudi, 1974: On the correct use of the wet adiabatic lapse rate in stability criteria of a saturated atmosphere. *J. Appl. Meteor.,* **13,** 318–324, doi:10.1175/1520-0450(1974)013<0318:OTCUOT>2.0.CO;2.

Laprise, J. P. R., and A. Plante, 1995: A class of semi-Lagrangian integrated-mass (SLIM) numerical transport algorithms. *Mon. Wea. Rev.,* **123,** 553–565, doi:10.1175/1520-0493(1995)123<0553:ACOSLI>2.0.CO;2.

Lauritzen, P. H., E. Kaas, and B. Machenhauer, 2006: A mass-conservative semi-implicit semi-Lagrangian limited-area shallow-water model on the sphere. *Mon. Wea. Rev.,* **134,** 1205–1221, doi:10.1175/MWR3115.1.

——, R. D. Nair, and P. A. Ullrich, 2010: A conservative semi-Lagrangian multi-tracer transport scheme (CSLAM) on the cubed-sphere grid. *J. Comput. Phys.,* **229,** 1401–1424, doi:10.1016/j.jcp.2009.10.036.

Lilly, D. K., 1978: A severe downslope windstorm and aircraft turbulence event induced by a mountain wave. *J. Atmos. Sci.,* **35,** 59–77, doi:10.1175/1520-0469(1978)035<0059:ASDWAA>2.0.CO;2.

Machenhauer, B., and M. Olk, 1997: The implementation of the semi-implicit scheme in cell-integrated semi-Lagrangian models. *Atmos.–Ocean,* **35** (Suppl. 1), 103–126, doi:10.1080/07055900.1997.9687344.

Melvin, T., M. Dubal, N. Wood, A. Staniforth, and M. Zerroukat, 2010: An inherently mass-conserving iterative semi-implicit semi-Lagrangian discretization of the non-hydrostatic vertical-slice equations. *Quart. J. Roy. Meteor. Soc.,* **136,** 799–814, doi:10.1002/qj.603.

Miglietta, M., and R. Rotunno, 2005: Simulations of moist nearly neutral flow over a ridge. *J. Atmos. Sci.,* **62,** 1410–1427, doi:10.1175/JAS3410.1.

Müller, E. H., and R. Scheichl, 2014: Massively parallel solvers for elliptic partial differential equations in numerical weather and climate prediction. *Quart. J. Roy. Meteor. Soc.,* **140,** 2608–2624, doi:10.1002/qj.2327.

Nair, R., and B. Machenhauer, 2002: The mass-conservative cell-integrated semi-Lagrangian advection scheme on the sphere. *Mon. Wea. Rev.,* **130,** 649–667, doi:10.1175/1520-0493(2002)130<0649:TMCCIS>2.0.CO;2.

Peltier, W. R., and T. L. Clark, 1979: The evolution and stability of finite-amplitude mountain waves. Part II: Surface wave drag and severe downslope windstorms. *J. Atmos. Sci.,* **36,** 1498–1529, doi:10.1175/1520-0469(1979)036<1498:TEASOF>2.0.CO;2.

——, and ——, 1983: Nonlinear mountain waves in two and three spatial dimensions. *Quart. J. Roy. Meteor. Soc.,* **109,** 527–548, doi:10.1002/qj.49710946106.

Pinty, J. P., R. Benoit, E. Richard, and R. Laprise, 1995: Simple tests of a semi-implicit semi-Lagrangian model on 2D mountain wave problems. *Mon. Wea. Rev.,* **123,** 3042–3058, doi:10.1175/1520-0493(1995)123<3042:STOASI>2.0.CO;2.

Rancic, M., 1992: Semi-Lagrangian piecewise biparabolic scheme for two-dimensional horizontal advection of a passive scalar. *Mon. Wea. Rev.,* **120,** 1394–1406, doi:10.1175/1520-0493(1992)120<1394:SLPBSF>2.0.CO;2.

Rivest, C., A. Staniforth, and A. Robert, 1994: Spurious resonant response of semi-Lagrangian discretizations to orographic forcing: Diagnosis and solution. *Mon. Wea. Rev.,* **122,** 366–376, doi:10.1175/1520-0493(1994)122<0366:SRROSL>2.0.CO;2.

Robert, A., 1981: A stable numerical integration scheme for the primitive meteorological equations. *Atmos.–Ocean,* **19,** 35–46, doi:10.1080/07055900.1981.9649098.

——, T. Yee, and H. Ritchie, 1985: A semi-Lagrangian and semi-implicit numerical-integration scheme for multilevel atmospheric models. *Mon. Wea. Rev.,* **113,** 388–394, doi:10.1175/1520-0493(1985)113<0388:ASLASI>2.0.CO;2.

Schär, C., D. Leuenberger, O. Fuhrer, D. Lüthi, and C. Girard, 2002: A new terrain-following vertical coordinate formulation for atmospheric prediction models. *Mon. Wea. Rev.,* **130,** 2459–2480, doi:10.1175/1520-0493(2002)130<2459:ANTFVC>2.0.CO;2.

Skamarock, W. C., and J. B. Klemp, 1994: Efficiency and accuracy of the Klemp–Wilhelmson time-splitting technique. *Mon. Wea. Rev.,* **122,** 2623–2630, doi:10.1175/1520-0493(1994)122<2623:EAAOTK>2.0.CO;2.

——, P. K. Smolarkiewicz, and J. B. Klemp, 1997: Preconditioned conjugate-residual solvers for Helmholtz equations in nonhydrostatic models. *Mon. Wea. Rev.,* **125,** 587–599, doi:10.1175/1520-0493(1997)125<0587:PCRSFH>2.0.CO;2.

Smith, R. B., 1979: The influence of mountains on the atmosphere. *Advances in Geophysics,* Vol. 21, Academic Press, 87–230, doi:10.1016/S0065-2687(08)60262-9.

——, 1980: Linear theory of stratified hydrostatic flow past an isolated mountain. *Tellus,* **32A,** 348–364, doi:10.1111/j.2153-3490.1980.tb00962.x.

Smolarkiewicz, P., and J. Pudykiewicz, 1992: A class of semi-Langragian approximations for fluids. *J. Atmos. Sci.,* **49,** 2082–2096, doi:10.1175/1520-0469(1992)049<2082:ACOSLA>2.0.CO;2.

Ullrich, P. A., P. H. Lauritzen, and C. Jablonowski, 2013: Some considerations for high-order 'incremental remap'-based transport schemes: Edges, reconstructions, and area integration. *Int. J. Numer. Methods Fluids,* **71,** 1131–1151, doi:10.1002/fld.3703.

Wong, M., W. C. Skamarock, P. H. Lauritzen, and R. B. Stull, 2013: A cell-integrated semi-Lagrangian semi-implicit shallow-water model (CSLAM-SW) with conservative and consistent transport. *Mon. Wea. Rev.,* **141,** 2545–2560, doi:10.1175/MWR-D-12-00275.1.

——, ——, ——, J. B. Klemp, and R. B. Stull, 2014: A compressible nonhydrostatic cell-integrated semi-Lagrangian semi-implicit solver (CSLAM-NH) with consistent and conservative transport. *Mon. Wea. Rev.,* **142,** 1669–1687, doi:10.1175/MWR-D-13-00210.1.

Xue, M., K. K. Droegemeier, and V. Wong, 2000: The Advanced Regional Prediction System (ARPS)—A multi-scale nonhydrostatic atmospheric simulation and prediction model. Part I: Model dynamics and verification. *Meteor. Atmos. Phys.,* **75,** 161–193, doi:10.1007/s007030070003.

Zerroukat, M., N. Wood, and A. Staniforth, 2002: SLICE: A semi-Lagrangian inherently conserving and efficient scheme for transport problems. *Quart. J. Roy. Meteor. Soc.,* **128,** 2801–2820, doi:10.1256/qj.02.69.

Zhang, K., H. Wan, B. Wang, and M. Zhang, 2008: Consistency problem with tracer advection in the atmospheric model GAMIL. *Adv. Atmos. Sci.,* **25,** 306–318, doi:10.1007/s00376-008-0306-z.